ON THE FAINT-END OF THE GALAXY LUMINOSITY FUNCTION IN THE EPOCH OF REIONIZATION: UPDATED CONSTRAINTS FROM THE *HST* FRONTIER FIELDS

B. YUE,[1] M. CASTELLANO,[2] A. FERRARA,[3,4] A. FONTANA,[2] E. MERLIN,[2] R. AMORÍN,[5,6] A. GRAZIAN,[2] E. MÁRMOL-QUERALTO,[7] M. J. MICHAŁOWSKI,[8] A. MORTLOCK,[7] D. PARIS,[2] S. PARSA,[7] S. PILO,[2] P. SANTINI,[2] AND M. DI CRISCIENZO[2]

[1]*National Astronomical Observatories, Chinese Academy of Sciences, 20A Datun Road, Chaoyang District, Beijing, 100012, China*

[2]*INAF - Osservatorio Astronomico di Roma, Via Frascati 33, I -00078Monte Porzio Catone (RM), Italy*

[3]*Scuola Normale Superiore, Piazza dei Cavalieri 7, I-56126 Pisa, Italy*

[4]*Kavli IPMU (WPI), Todai Institutes for Advanced Study, the University of Tokyo, Japan*

[5]*Cavendish Laboratory, University of Cambridge, 19 JJ Thomson Avenue, Cambridge, CB3 0HE, UK*

[6]*Kavli Institute for Cosmology, University of Cambridge, Madingley Road, Cambridge CB3 0HA, UK*

[7]*SUPA, Scottish Universities Physics Alliance, Institute for Astronomy, University of Edinburgh, Royal Observatory, Edinburgh, EH9 3HJ, U.K.*

[8]*Astronomical Observatory Institute, Faculty of Physics, Adam Mickiewicz University, ul. Słoneczna 36, 60-286 Poznań, Poland*

ABSTRACT

Ultra-faint galaxies are hosted by small dark matter halos with shallow gravitational potential wells, hence their star formation activity is more sensitive to feedback effects. The shape of the faint-end of the high-z galaxy luminosity function (LF) contains important information on star formation and its interaction with the reionization process during the Epoch of Reionization (EoR). High-z galaxies with $M_{\rm UV} \gtrsim -17$ have only recently become accessible thanks to the Frontier Fields (FFs) survey combining deep *HST* imaging and the gravitational lensing effect. In this paper we investigate the faint-end of the LF at redshift >5 using the data of FFs clusters Abell 2744 (A2744), MACSJ0416.1-2403 (M0416), MACSJ0717.5+3745 (M0717) and MACSJ1149.5+2223 (M1149). We analyze both an empirical and a physically-motivated LF model to obtain constraints on a possible turn-over of LF at faint magnitudes. In the empirical model the LF drops fast when the absolute UV magnitude $M_{\rm UV}$ is much larger than a turn-over absolute UV magnitude $M_{\rm UV}^{\rm T}$. We obtain $M_{\rm UV}^{\rm T} \gtrsim -14.6$ (15.2) at 1 (2) σ confidence level (C.L.) for $z \sim 6$. In the physically-motivated analytical model, star formation in halos with circular velocity below v_c^* is fully quenched if these halos are located in ionized regions. Using updated lensing models and new additional FFs data, we re-analyze previous constraints on v_c^* and $f_{\rm esc}$ presented by Castellano et al. 2016a (C16a) using a smaller dataset. We obtain new constraints on $v_c^* \lesssim 59$ km s^{-1} and $f_{\rm esc} \lesssim 56\%$ (both at 2σ C.L.) and conclude that there is no turn-over detected so far from the analyzed FFs data. Forthcoming *JWST* observations will be key to tight these constraints further.

Keywords: dark ages, reionization, first stars — galaxies: high-redshift — gravitational lensing: strong

1. INTRODUCTION

During the Epoch of Reionization (EoR, $6 \lesssim z \lesssim 30$), the intergalactic medium (IGM) was gradually ionized by energetic photons mainly emitted by the first galaxies. This in turn leads to the suppression of star formation in small galaxies, because their host halos hardly collect gas from ionized environment. This feedback effect raises the following questions: How faint the first galaxies could be and which halos could sustain star formation activity during the EoR?

According to the hierarchical structure formation scenario, smaller dark matter halos are much more common than bigger ones in the Universe, resulting in an overwhelming numerical abundance of very faint galaxies (Mason et al. 2015; Mashian et al. 2016; Finlator et al. 2017; Liu et al. 2016). Thereby, faint galaxies are promising candidates as main sources of reionizing photons (e.g. Bouwens et al. 2015a; Robertson et al. 2015; Castellano et al. 2016b), with a crucial contribution possibly coming from objects far below the detection limits of even the deepest existing surveys (Salvaterra et al. 2011; Robertson et al. 2013; Choudhury et al. 2008; Choudhury & Ferrara 2007; Dayal et al. 2013; Salvaterra et al. 2013). Moreover, faint galaxies are less clustered and their environment gas is less clumped, therefore they are more effective in reionizing the IGM.

To understand the role of star-forming galaxies in the reionization process, it is thus crucial to constrain their number density and star-formation efficiency by studying the UV luminosity function (LF) down to the faintest limits. The faint-end of the UV LF at high redshift has been found to have a steep slope at least down to absolute UV magnitudes $M_{\rm UV} \sim -16$ (McLure et al. 2013; Bouwens et al. 2015b, B15 hereafter) in blank fields or even $M_{\rm UV} \sim -12$ in gravitational lensing fields (Livermore et al. 2017, however see Bouwens et al. 2017b, these two are L17 and B17 hereafter). The high-z LFs have also been reconstructed from the number of ultra-faint dwarf galaxies – some of which are believed fossils of reionization galaxies – in the Local Group. For example, Weisz et al. (2014) conclude that the LF at $z \sim 5$ does not have any break at least down to $M_{\rm UV} \sim -10$. At the same time, the detection of a break or turn-over would have an important implication related to the nature of the first galaxies and their contribution to reionization (e.g. Giallongo et al. 2015; Madau & Haardt 2015; Mitra et al. 2016).

Star formation in dark matter halos relies on the gas cooling process. However, both supernova explosion and ionizing radiation could prevent cooling. These feedback effects reduce the efficiency of star formation (Dayal et al. 2013; Xu et al. 2016; Sun & Furlanetto 2016) or even completely quench it, if the halo mass is too small. As a result, the number of galaxies hosted by small halos drops and we expect to see a "turn-over" in the faint-end of the galaxy LFs (Yue et al. 2016, Y16 hereafter). For example, in the "Cosmic Reion-

ization on Computers" (CROC) project, by galaxy formation and radiative transfer numerical simulations, it is found that the UV LF turns over at $M_{\rm UV} \sim -14$ to ~ -12 (Gnedin 2016). And in the "FirstLight" project with radiative feedback effects, the LF has a flattening at $M_{\rm UV} \gtrsim -14$ (with host halos' circular velocity ~ 30 - 40 km s^{-1}, Ceverino et al. 2017). Modifications of the initial power spectrum as in WDM cosmologies can also have a similar effect, see e.g. Dayal et al. (2015); Menci et al. (2016, 2017). Observations of galaxies around the turn-over would greatly increase our knowledge of the star formation physics in galaxies contributing most to reionization, and may directly answer our questions in the first paragraph (Yue et al. 2014).

Until now, there is no evidence that confirms or rules out the existence of such turn-over in both regular surveys and in gravitational lensing surveys, probably because the turn-over magnitude is still fainter than the limiting magnitudes of current measurements, see e.g. McLure et al. (2013); B15; Atek et al. (2015b); Atek et al. (2015a) (A15 hereafter); L17; Laporte et al. (2016); Ishigaki et al. (2017) (I17 hereafter).

With the help of strong magnification effects, the gravitational lensing provides an opportunity to detect galaxies below the detection limits of regular surveys. However, the cost is that the survey volume is reduced, and lensing models introduce extra uncertainties into the recovered intrinsic brightness of observed galaxies (B17).

The Frontier Fields (FFs) survey observed six massive galaxy clusters and their parallel fields in optical and near-infrared bands with the *Hubble*[1] and *Spitzer*[2] space telescopes (Lotz et al. 2017). These observations were also followed up by other observatories at longer and shorter wavelengthes, e.g. *ALMA* (González-López et al. 2017a,b) and *Chandra* (Ogrean et al. 2015, 2016; van Weeren et al. 2017). Using the clusters as lenses, these images are deep enough to unveil faint galaxy populations at the EoR.

In Y16, we have derived the form of the LF faint-end during and after the EoR by assuming that the star formation in halos with circular velocity below a threshold v_c^* and located in ionized bubbles is quenched, where v_c^* is a free parameter. In Castellano et al. (2016a) (C16a hereafter) we constrained $v_c^* \lesssim 60$ km s^{-1} (2σ C.L.) by using the observed number counts of ultra-faint galaxies in two of the six FFs cluster fields, A2744 and M0416, and the *Planck* 2015 results for τ (Planck Collaboration et al. 2016a).

Recently, by using two FFs clusters Abell 2744 (A2744) and MACSJ0416.1-2403 (M0416), L17 found that the faint-end of the LF at $z \sim 6$ always has steep slope ($\alpha \sim -2$) and

---

does not turn over at $\gtrsim -12.5$. Generally it is expected that at higher redshift the turn over magnitude is fainter, because at the earlier reionization stage the radiative feedback effects should be weaker, and halos at higher redshift are more concentrated and easier to hold their gas. Therefore from L17 results it can be reasonably inferred that during the EoR ($z > 6$), the LF faint-end slope is steep even at magnitudes fainter than -12.5. If this is the case, the galaxies that ionized the Universe have already been uncovered (Robertson et al. 2013, 2015). However, their result was questioned by B17 who argued that L17 may overestimate the volume density at the faint end due to: 1) an excess of sources near the completeness limit; and 2) the assumption of too large intrinsic half-light radii.

B17 investigated the impact of magnification errors on the LF carefully and found that at $M_{\rm UV} \gtrsim -14$ the systematic differences of magnifications from different lensing models are extremely high. They developed a new model that incorporates the magnification errors into the LF, and by analyzing four FFs clusters: A2744, M0416 plus MACSJ0717.5+3745 (M0717) and MACSJ1149.5+2223 (M1149) they obtained the constraints that the LF should not turn over at least at $M_{\rm UV} < -15.3$ to -14.2 (1σ C.L.), consistent with C16a.

In this paper, we expand the analysis presented in C16a by adding new FFs data and improved lensing models to obtain number counts in the two additional FFs clusters and update the previous two clusters. Throughout this paper we use the following cosmological parameters: $\Omega_m = 0.308, \Omega_\Lambda = 0.692, \Omega_b = 0.048, h = 0.678, \sigma_8 = 0.815, n_s = 0.97$ (Planck Collaboration et al. 2016a), magnitudes are presented in AB system.

2. METHODS

2.1. *Observations*

The photometric catalogues of high-z galaxies used in the present paper are provided by the ASTRODEEP team (Castellano et al. 2016c; Merlin et al. 2016b; Di Criscienzo et al. 2017), and all the lensing models are provided by the FFs team on the project website[3].

The high-z sample comprises all sources with $H_{160,\rm int} \geq 27.5$ from the ASTRODEEP catalogs of FFs clusters A2744, M0416 (Merlin et al. 2016b; Castellano et al. 2016a), M0717 and M1149 (Di Criscienzo et al. 2017)[4], where $H_{160,\rm int}$ is the demagnified apparent magnitude at the *HST* F160W band (H band). The model described in Sec. 2.2 will use sample

---

[3] https://archive.stsci.edu/prepds/frontier/lensmodels/

[4] Download: http://www.astrodeep.eu/frontier-fields-download/;
Catalogue interface: http://astrodeep.u-strasbg.fr/ff/index.html

galaxies with $5.0 < z < 7.0$, while the model described in Sec. 2.3 will use sample galaxies with $5.0 < z < 9.5$, see details in the relevant sections. The original samples presented by ASTRODEEP team have redshifts up to ~ 10. However for objects $z \gtrsim 9.5$, their redshifts may be not correctly measured. Moreover, samples with $z \gtrsim 9.5$ are only detectable in one band. Considering these reasons we do not select samples with $z > 9.5$.

All catalogues include photometry from the available *HST* ACS and WFC3 bands (B435, V606, I814, Y105, J125, JH140, H160, see e.g. Lotz et al. 2017) and from deep K-band (Brammer et al. 2016) and IRAC 3.6 μm and 4.5 μm data (PI Capak). Sources are detected on the H160 band after removing foreground light both from bright cluster galaxies and the diffuse intra-cluster light (ICL) as described in detail in Merlin et al. (2016b). Foreground light is also removed from the *HST* bands before estimating photometry with SExtractor (Bertin & Arnouts 1996) in dual-image mode. Photometry from the lower resolution Ks and IRAC images has been obtained with T-PHOT v2.0 (Merlin et al. 2015, 2016a). Photometric redshifts for all the sources have been measured with six different techniques based on different codes and assumptions. The FFs sources are then assigned the median of the six available photometric redshift estimates in order to minimize systematics and improve the accuracy. The final typical error on the photo-z is $\sim 0.04 \times (1 + z)$ (Castellano et al. 2016a; Di Criscienzo et al. 2017). For the four clusters A2744, M0416, M0717 and M1149, the apparent magnitudes brighter than which more than 10% point-like objects could be successfully resolved are 28.8, 28.8, 28.5 and 28.7 respectively.

In the top panel of Fig. 1 we plot the observed H band apparent magnitude, H_{160}, vs. redshift for our selected sample galaxies (galaxies with photometric redshift between 5.0 and 9.5 and with demagnified H band magnitude larger than 27.5 in either of lensing models) in the four FFs clusters. There are 73 (87), 51 (62), 73 (76) and 34 (47) galaxies with $5.0 < z < 7.0$ ($5.0 < z < 9.5$) in clusters A2744, M0416, M0717 and M1149 respectively. In the Tab. A1 in the Appendix A we list the unique ID in the ASTRODEEP catalog of all these objects, so that their properties like the released SEDs could be found directly in the website.

The magnification for each observed source is estimated on the basis of the relevant photometric redshift from shear and mass surface density values at its barycenter of the light distribution. All models made available on the STSCI website [5] are used.

Compared to C16a we update in this paper the A2744 and M0416 high-z samples by exploiting the improved v3 lensing

---

[5] http://www.stsci.edu/hst/campaigns/frontier-fields/Lensing-Models

models now available, and we include in the analysis number counts from other two additional clusters, M0717 and M1149. In Tab. 1 we list the clusters and the corresponding lensing models used in this paper. In Fig. 2 we plot the distributions of the magnification factors of our selected galaxy samples in each cluster, for our adopted lensing models. In different lensing models an identified galaxy could have different magnifications, hence different demagnified magnitudes. Therefore for a given cluster we can reconstruct different number counts (galaxy number per magnitude bin) when using different lensing models. We make the median of these counts as our fiducial number counts. In middle and bottom panels of Fig. 1 we show the number counts of the faint ($H_{160,\mathrm{int}} > 27.5$) galaxies with $5.0 < z < 7.0$ and $5.0 < z < 9.5$ in the fields of four FFs clusters (we do not use the data of the parallel blank fields), as a function of $H_{160,\mathrm{int}}$.

2.2. An empirical description of the LF turn-over

Is there evidence of a "turn-over" in the faint-end of the high-z galaxy LFs from the available FFs data? To investigate this problem we adopt the following reference LF model – a standard Schechter formula modulated by a term that rapidly drops when the absolute UV magnitude M_{UV} is much fainter than the turn-over magnitude $M_{\mathrm{UV}}^{\mathrm{T}}$, and rapidly approaches unity when $M_{\mathrm{UV}} \ll M_{\mathrm{UV}}^{\mathrm{T}}$:

$$\Phi(M_{\mathrm{UV}}, z) = 0.4\ln(10)\Phi^* \exp[10^{-0.4(M_{\mathrm{UV}}-M_{\mathrm{UV}}^*)}]$$
$$\times 10^{-0.4(1+\alpha)(M_{\mathrm{UV}}-M_{\mathrm{UV}}^*)}0.5[(1-\mathrm{erf}(M_{\mathrm{UV}}-M_{\mathrm{UV}}^{\mathrm{T}})], \tag{1}$$

where *erf* is the error function. At the $M_{\mathrm{UV}}^{\mathrm{T}}$ the LF drops to half the value of a standard Schechter LF. In addition to the three redshift-dependent Schechter parameters Φ^*, M_{UV}^*, α, we introduce here a new one parameter $M_{\mathrm{UV}}^{\mathrm{T}}$. The M_{UV}^* is mainly determined by observations of bright galaxies and by large volume galaxy surveys while it is unconstrained in our lensed samples of ultra-faint galaxies. For this reason, and to focus on the LF turn-over relevant parameters only, we directly adopt the parameterization of M_{UV}^* from Sec. 5.1 of Bouwens et al. (2015b):

$$M_{\mathrm{UV}}^* = -20.95 + 0.01 \times (z-6), \tag{2}$$

discarding its uncertainties. We keep the Φ_* and α as free parameters that will be constrained together with $M_{\mathrm{UV}}^{\mathrm{T}}$ from the FFs data.

2.3. A physically-motivated model of the high-z galaxy LFs

In Y16 we have developed a physically-motivated analytical model that describes the faint-end of the high-z galaxy LFs during the EoR. The model calibrates the "star formation efficiency" (defined as the star formation rate to halo dark matter mass ratio) - halo mass relation using the Schechter
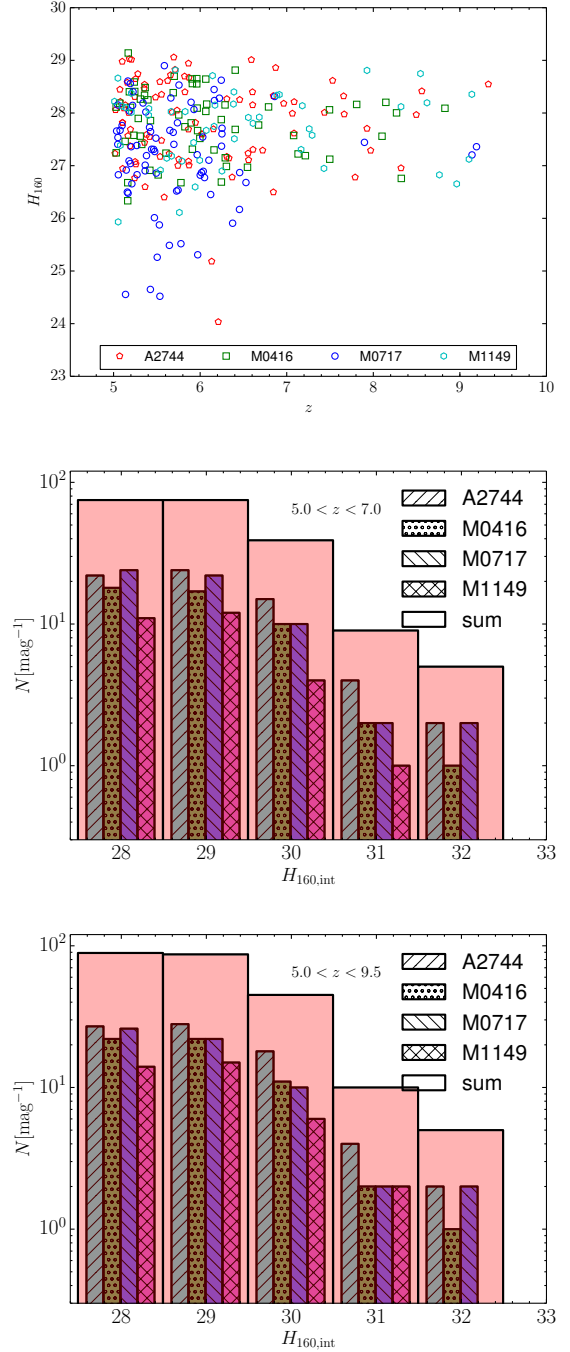

Figure 1. *Top:* The observed H band magnitudes vs. redshift of the sample galaxies with photometric redshifts between 5.0 and 9.5 in the four FFs clusters respectively. *Middle and bottom:* The galaxy number counts between $z = 5.0 - 7.0$ and $z = 5.0 - 9.5$ vs. demagnified H band apparent magnitude for the four FFs clusters. For each cluster we plot the median of the number counts reconstructed using lensing models listed in Tab. 1. We also plot the sum of the four clusters. Histograms in same group are in the same magnitude bin, for displaying purpose we shift their x-coordinates.

Table 1. The FFs clusters and lensing models used in this paper.

Cluster	Lensing model
Abell 2744 (A2744)	GLAFIC v3; Sharon v3; Williams v3; Zitrin-LTM-Gauss v3;Zitrin-NFW v3; CATS v3.1
MACSJ0416.1-2403 (M0416)	GLAFIC v3; Sharon v3; Williams v3.1; Zitrin-LTM-Gauss v3; Zitrin-LTM v3; CATS v3.1; Bradač v3; Diego v3
MACSJ0717.5+3745 (M0717)	GLAFIC v3; Sharon v2; Williams v1; Zitrin-LTM-Gauss v1; Zitrin-LTM v1; CATS v1; Bradač v1; Merten v1
MACSJ1149.5+2223 (M1149)	GLAFIC v3; Sharon v2.1; Williams v1; Zitrin-LTM-Gauss v1; Zitrin-LTM v1; CATS v1; Bradač v1; Merten v1

Relevant references for lensing models listed in the table: GLAFIC: Kawamata et al. (2017, 2016); Ishigaki et al. (2015); Oguri (2010). Sharon: Johnson et al. (2014); Jullo et al. (2007). Williams: Priewe et al. (2017); Sebesta et al. (2016); Grillo et al. (2015); Jauzac et al. (2014); Mohammed et al. (2014); Liesenborgs et al. (2006). Zitrin: Zitrin et al. (2013, 2009). CATS: Jauzac et al. (2015, 2014); Richard et al. (2014); Jauzac et al. (2012); Jullo & Kneib (2009). Bradač: Hoag et al. (2016); Bradač et al. (2009, 2005). Diego: Diego et al. (2015, 2007, 2005b,a). Merten: Merten et al. (2011, 2009). All models are available on the STSCI website.
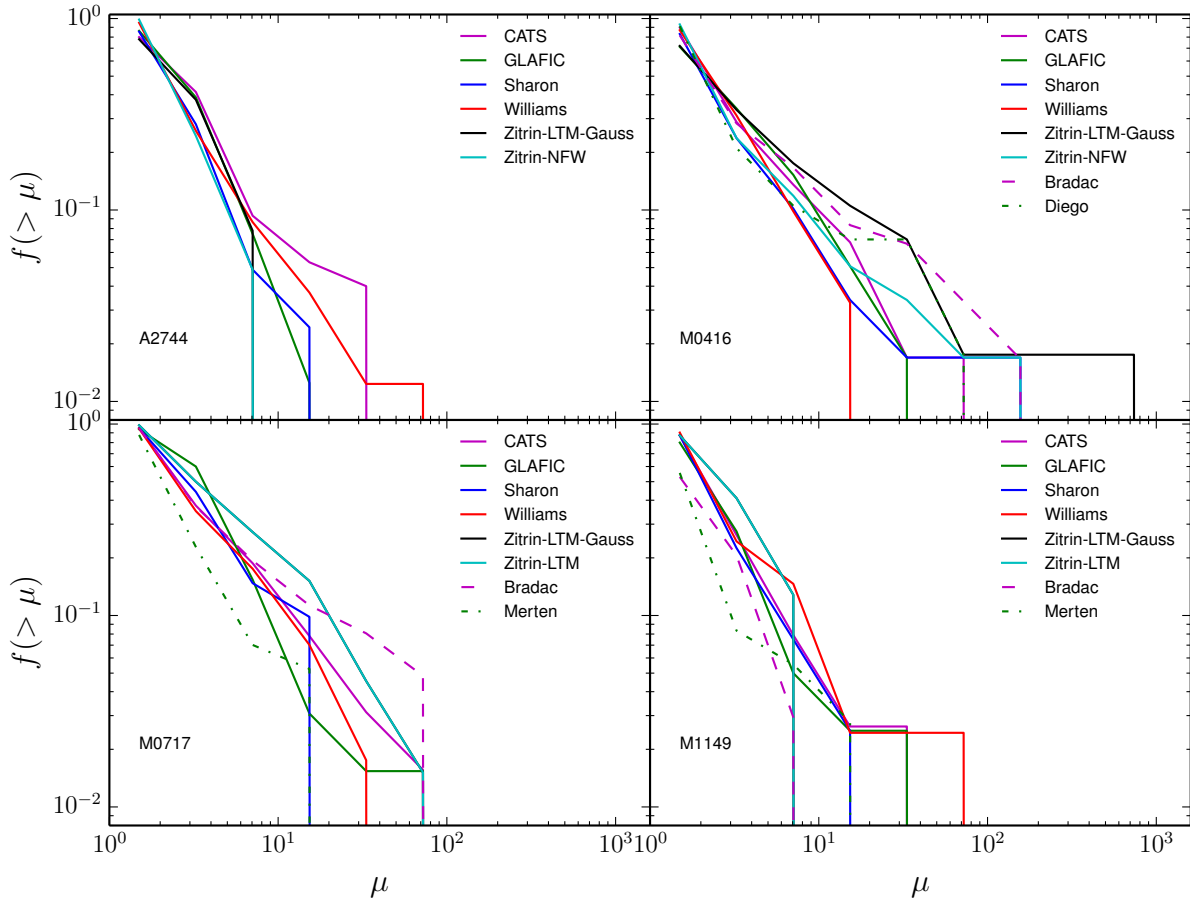

Figure 2. The distributions of the magnification factors of galaxies with photometric redshifts between redshift 5.0 and 9.5 in each cluster and $H_{160,\text{int}}$ in either of lensing models.

formula of observed LF at redshift ~ 5, then computes the luminosity of a halo according to its mass and formation time at any redshifts (Mason et al. 2015, see also Trenti et al. 2010 and Tacchella et al. 2013). Considering the probability distribution of a halo's formation time (Giocoli et al. 2007), and the possibility of its star formation being quenched (if the circular velocity of this halo is smaller than a pre-assumed circular velocity criterion v_c^* and it is located in ionized re-

gions), the LF is then derived from halo mass function. In this model, the LF does not necessarily decrease monotonically at its faint end but have complex shapes, see Fig. 6 and Fig. 7 in Y16.

The Y16 model has two free parameters, the escape fraction of ionizing photons, f_{esc}, and the critical circular velocity, v_c^*. The galaxy number counts are sensitive to v_c^* but less sensitive to f_{esc}, therefore we combine the number counts

with the measured Thomson scattering optical depth to CMB photons, τ, to obtain the joint constraints.

2.4. *Statistical framework*

Here we summarise the procedure adopted to derive constraints on theoretical parameters from the observed galaxy number counts. A more detailed discussion can be found in C16a.

The sample galaxies of each cluster in the specified redshift range are divided into n_b bins according to their demagnified magnitudes. Suppose in the ith bin there are $N_{\rm obs}^i$ galaxies. For given luminosity function model with parameter set **a**, we perform Monte Carlo simulations to calculate the probability to observe such number of galaxies in this bin, $p_1(N_{\rm obs}^i|\mathbf{a})$. In the Monte Carlo simulations, we include the completeness as a function size and magnitude of the image. The image size of each input galaxy is derived from its luminosity by using an intrinsic galaxy radius - luminosity relation given in Huang et al. (2013). This relation is comparable with the relation in Bouwens et al. (2017a,b). We note that Kawamata et al. (2017) found a steeper relation slope for galaxies down to $M_{\rm UV} \sim -12.3$ in FFs, although at this moment we do not check the influence on our results. $p_1(N_{\rm obs}^i|\mathbf{a})$ depends on both luminosity function models and lensing models. We use the mean probability of different lensing models (see their Eq. 3) except when comparing different lensing models.

We then build the following combined likelihood:

$$L = L_1 \times L_2$$
$$= \left[\prod_i^{n_b} p_1(N_{\rm obs}^i|\mathbf{a})\right] \times L_2, \qquad (3)$$

where L_1 is the likelihood from our FFs observations, and L_2 is the likelihood of additional observations that can help to improve the constraints.

For the empirical model, we build L_2 from the constructed LF data points of wide blank fields at $z \sim 6$,

$$L_2 = \prod_j \frac{1}{\sqrt{2\pi\sigma_{\Phi,j}^2}} \exp\left[-\frac{(\Phi_j - \Phi(\mathbf{a}))^2}{2\sigma_{\Phi,j}^2}\right]. \qquad (4)$$

Introducing this L_2 is necessary, because although the gravitational lensing surveys are deeper, usually they have smaller effective volume, while the blank field surveys have large volume, thereby are helpful for reducing the uncertainties.

For the physically-motivated model, we build the L_2 from the measured CMB scattering optical depth,

$$L_2(\mathbf{a}) = \frac{1}{\sqrt{2\pi\sigma_\tau^2}} \exp\left[-\frac{(\tau_{\rm obs} - \tau(\mathbf{a}))^2}{2\sigma_\tau^2}\right]. \qquad (5)$$

The constraints on parameter set **a** are obtained by looking for the minimum of $\chi^2 = -2\log(L)$ and its variations corresponding to different C.L. given by chi square distribution.

3. RESULTS

3.1. *Is a LF turn-over observed at $z \sim 6$?*

In this subsection we investigate the constraints on parameters in the empirical model described in Sec. 2.2 at $z \sim 6$ by analyzing galaxy samples with $5 < z < 7$ in ASTRODEEP catalogs.

Using a collection of wide and deep blank field *HST* surveys data, including the CANDELS, HUDF09, HUDF12, ERS and BoRG/HIPPIES fields, Bouwens et al. (2015b) (B15) have constructed the LFs from $z \sim 4$ to $z \sim 10$. We use their stepwise maximum likelihood determination of the $z \sim 6$ data points to build the L_2 (see Table 5 of B15). We vary Φ_* in the range $\Phi_* \leq 1.5 \times 10^{-3}$ Mpc^{-3}, α in the range $-2.5 \leq \alpha \leq -1.6$ and $M_{\rm UV}^{\rm T}$ in the range $-18 \leq M_{\rm UV}^{\rm T} \leq -10$.

The constraints on empirical model parameters are shown in Fig. 3. In the 2D $M_{\rm UV}^{\rm T}$-α contour map, the Φ_* has been marginalized, and in the $M_{\rm UV}^{\rm T}$-Φ_* contour map the α has been marginalized. We can see that the upper boundary of $M_{\rm UV}^{\rm T}$ is always open. To obtain the final constraints we marginalize both Φ_* and α, and we have $M_{\rm UV}^{\rm T} \gtrsim -14.6$ at 1σ C.L. and $M_{\rm UV}^{\rm T} \gtrsim -15.2$ at 2σ C.L.. Still, we only find the lower boundary of $M_{\rm UV}^{\rm T}$, the upper boundary is open. This implies that no evidence is found in the existing data for the four FFs clusters of a LF turn-over at $z \approx 6$. We summarise the constraints in Tab. 2. We have tested that in Eq. (3) if we use the L_2 derived from Finkelstein et al. (2015) LF at $z \sim 6$ we obtained quite similar results on $M_{\rm UV}^{\rm T}$. If we remove L_2, i.e. using only the FFs data, while we restrict Φ_*, α and $M_{\rm UV}^{\rm T}$ vary in range specified in last paragraph, we obtain $M_{\rm UV}^{\rm T} \gtrsim -15.2$ and $M_{\rm UV}^{\rm T} \gtrsim -15.9$ at 1σ and 2σ C.L. respectively.

We plot the LF corresponding to the constraints at $z \sim 6$ in Fig. 4 by curves and filled regions. As a reference and consistency check, we also plot the B15 LF data, and the LF data constructed from A2744, M0416 and M0717 and their corresponding parallel blank filed in A15 at $z \sim 7$, which is one of the deepest LFs and consistent with other LFs in the overlap magnitude range. Moreover, the L17, B17 and I17 LFs are also plotted in Fig. 4.

Before making comparisons between B17 and our results, it is necessary to clarify a dissimilarity between the definition of the "turn-over magnitude" between B17 and our work. In B17, the turn-over magnitude is the absolute magnitude at which the LF's derivative is zero, while in our work it is defined as the absolute magnitude where the LF decreases to half of the Schechter LF. Moreover, their LF-end is modulated by a term $10^{-0.4\delta(M_{\rm UV}+16)^2}$ which could decrease gently even when $M_{\rm UV}$ is higher than the turn-over magnitude, depending on δ. However we assume the modulation term $0.5[1 - {\rm erf}(M_{\rm UV} - M_{\rm UV}^{\rm T})]$, at $M_{\rm UV} > M_{\rm UV}^{\rm T}$ the LF drops rapidly. For the above reason, we do not directly compare our $M_{\rm UV}^{\rm T}$ with B17. Instead, we plot our constrained LF together with
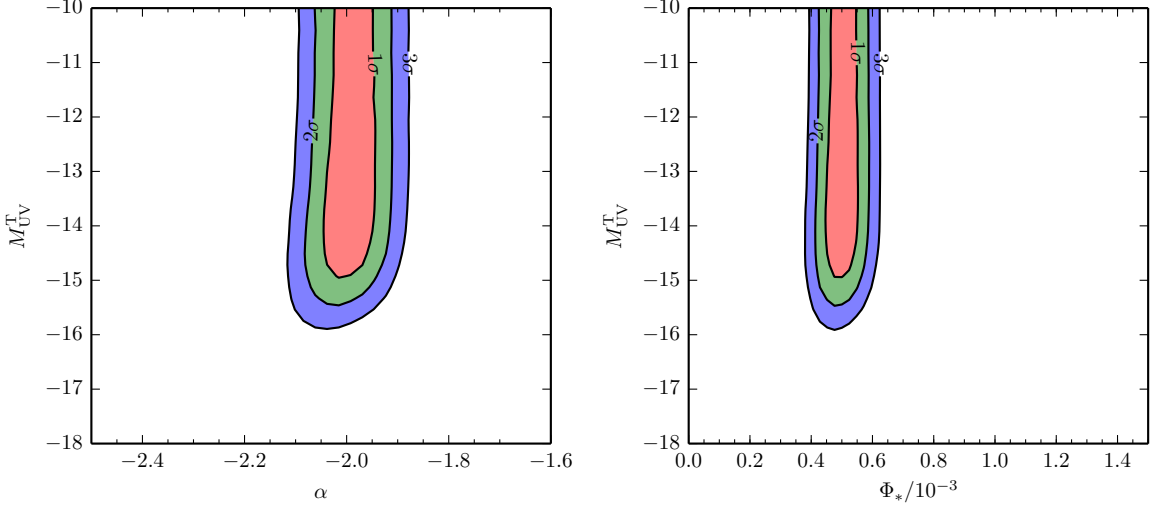
Figure 3. The constraints on α, Φ_* and M_{UV}^T from the combination of all the four FFs clusters. The panels are the α-M_{UV}^T and Φ_*-M_{UV}^T contour maps respectively. In each case the remaining parameter has been marginalized.
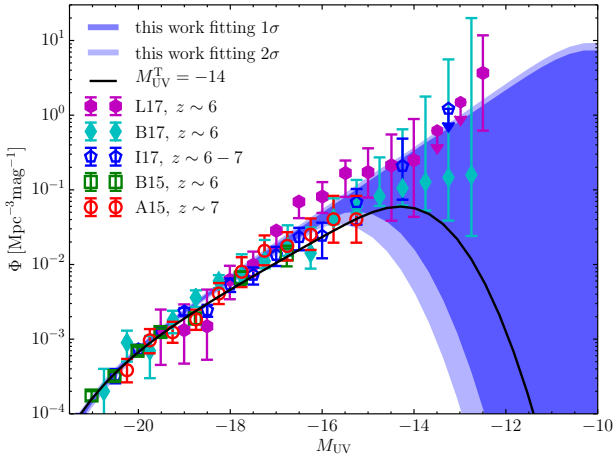

Figure 4. The LF constrained in our work. We show the uncertainties within 1σ and 2σ C.L. As comparisons we plot the B15, A15, B17, L17 and I17 observations together, and a theoretical LF with $M_{UV}^T = -14$.

the LF constructed in B17, see Fig. 4. From this figure, the B17 LF constraint could be approximately translated into $M_{UV}^T \gtrsim -14$ of our model, a bit deeper than what we found in our work, $M_{UV}^T \gtrsim -14.6$. This difference might be due to the different methodologies adopted to take into account systematic effects. We use the median of the number counts from different lensing models as the true number count, while B17 incorporates systematics estimated by the difference between the various models. As a check, in our work if we drop the galaxies with magnification factors > 100 in observations we obtain constraints $M_{UV}^T \gtrsim -14.8$ (-15.4) at 1σ (2σ) C.L., quite similar to the model without dropping galaxies.

The L17 constraint on LF turn-over is deeper than ours, i.e. no turn-over is seen until $M_{UV} \sim -12.5$ at $z \sim 6$ in their work. The difference between our results and L17 ones can be due to the different methodologies adopted: a) They build the source catalog and subtract the intra-cluster light in a very different way than in our case. b) They have assumed different galaxy size distributions. c) In our case, we first construct the number count for each lensing model independently, then take the median of the number counts reconstructed from different lensing models; while in L17, for the image of each galaxy they take the flux-weighted magnification of different lensing models, then construct the LF.

We now investigate the systematic differences between the various lensing models. In Fig. 5 we show the α-M_{UV}^T constraints by using only one lensing model each time, ignoring version discrepancies. Each of "GLAFIC", "CATS", "Sharon", "Williams" and "Zitrin-LTM-Gauss" is shown by one column in Fig. 5. We choose these five lensing models because they are available for all the four clusters; and at least for A2744 and M0416 the versions are equal or later than v3.0. For each lensing model from top to bottom the panels are α-M_{UV}^T constraints, the sum of the number counts for the four FFs clusters and the LFs corresponding to the constraints (see Tab. 2).

Indeed, the discrepancies between lensing models are rather evident, especially for the M_{UV}^T boundaries. This is because these lensing models use different mass distribution and observations as constraint inputs; as a results, although the number counts (the middle panels of Fig. 5) are basically consistent with each at $H_{160,\text{int}} \lesssim 32$, at the faintest end they are rather different from each other. Detailed investigations about the systematics among lensing models could be found in Priewe et al. (2017); Acebron et al. (2017); Meneghetti

et al. (2017) and the references of each lensing models listed below Tab. 1. In all the cases, the upper boundaries are open, implying that no turn-over is apparent.

In bottom panels of Fig. 5 we also plot the absolute magnitudes of the faintest galaxies in each lensing model by vertical lines. Usually the $M_{\rm UV}^{\rm T}$ constraints are shallower than these faintest magnitudes. We check the influence of the faintest galaxies on the $M_{\rm UV}^{\rm T}$ constraints. We find that for all lensing models except Williams discussed in Fig. 5, the faintest galaxies (referring to the demagnified magnitudes) are in the M0416 field. For the Williams model the faintest galaxy is in the M0717 field.

For the GLAFIC and CATS lensing models, the faintest galaxy is the same one whose observed apparent magnitude $H_{160} = 28.1$, and demagnified magnitudes $H_{160,{\rm int}} = 32.2$ and 32.9 in these two lensing models respectively. For Sharon, Williams and Zitrin-LTM-Gauss lensing model, the faintest galaxies have $H_{160} = 28.0$, 28.6 and 26.7, and $H_{160,{\rm int}} = 33.9$, 32.5 and 34.6 respectively. An investigation of the influence by the photometric errors is given in Appendix B.

Although we have checked all the galaxies one-by-one visually and do not find any reason to consider the above faint galaxies passed our checkup spurious objects, we still make a test to check their influences. In case including (removing) them in samples, we obtain the 2σ C.L. constraints: $M_{\rm UV}^{T} \gtrsim$ -15.2 (-15.3), -14.3 (-14.5), -14.7 (-15.5), -14.9 (-15.2), and -13.2 (-14.1) for lensing models GLAFIC, CATS, Sharon, Williams and Zitrin-LTM-Gauss respectively. The changes on the Sharon and Zitrin-LTM-Gauss model are most obvious, almost up to 1 magnitude.

3.2. *Constraints on v_c^**

We then investigate the constraints we can put on the physically-motivated model. Since in this model both $f_{\rm esc}$ and v_c^* are redshift independent parameters, we use all the data in $z = 5.0 - 9.5$. In top panel of Fig. 6 we show the constraints on $f_{\rm esc}$ and v_c^*, using the combination of galaxy number counts in the FFs fields and the latest *Planck*2016 Thomson scattering optical depth to CMB photons: $\tau = 0.058 \pm 0.012$ (Planck Collaboration et al. 2016b). Compared with C16a, the smaller τ helps us to obtain tighter constraints on $f_{\rm esc}$, say $f_{\rm esc} \lesssim 57\%$ (2σ C.L.) after marginalizing v_c^*. When marginalizing $f_{\rm esc}$ we find $v_c^* \lesssim 59$ km s^{-1} (2σ C.L.), which corresponds to a halo mass $M_h \lesssim 4.0 \times 10^9\ M_\odot$ and $9.2 \times 10^9\ M_\odot$ at $z = 9.5$ and 5 respectively. Given the halo mass, using the star formation efficiency - halo mass relation constructed in Y16, and the halo assembly history, we can derive its mean luminosity. We therefore translate the halo mass constraints into absolute UV magnitude constraints, $M_{\rm UV} \gtrsim -14.8$ and -15.0. They are slightly tighter than those reported in C16a (see Fig. 3 there). Additional constraints are listed in Tab. 2, where we present both 1σ and

2σ constraints. The LFs at $z \sim 6$ and 8 in Y16 model corresponding to no feedback, $v_c^* = 50$ and 59 km s^{-1} for $f_{\rm esc} = 0.15$ are shown in bottom panels of Fig. 6.

We also find that different clusters do not contribute equally to the final constraint. If we respectively *remove* one of A2744, M0416, M0717 and M1149 each time, we obtain $v_c^* \lesssim 65$, 61, 62 and 58 km s^{-1} (all at 2σ C.L.) respectively. As seen in Fig. 1, the M1149 has less contribution to the number counts in the faintest magnitude bin, therefore have smaller influence in the final constraint.

We also investigate the discrepancies between different lensing models in this case. When using one lensing model at a time, as mentioned in the last subsection, we obtain the 2σ C.L. constraints: $v_c^* \lesssim 56$ (GLAFIC), 49 (CATS), 56 (Sharon), 54 (Williams) and 45 (Zitrin-LTM-Gauss) km s^{-1} respectively, see Tab. 2.

4. CONCLUSIONS

We investigated the LF of galaxies in the reionization epoch at low luminosities under the explicit assumption that any deviation from a pure Schechter LF at faint magnitudes is imprinted by feedback effects during reionization itself. We considered two LF models, and obtained constraints on their parameters from the observed high-z ultra-faint galaxy number counts in four FFs gravitational lensing cluster fields. We first test an empirical model where the standard Schechter formula is modulated by the suppressing term $0.5[1 - {\rm erf}(M_{\rm UV} - M_{\rm UV}^{\rm T})]$. The LF is unchanged when $M_{\rm UV} \ll M_{\rm UV}^{\rm T}$, and drops rapidly when $M_{\rm UV} \gg M_{\rm UV}^{\rm T}$. Secondly, we consider the physically-motivated model proposed by Y16 and analysed in C16a. In this model the star formation is quenched in halos with circular velocity smaller than v_c^*, during and after the EoR, as long as they are located in ionized regions. As a result, the LF has complex behavior at low luminosities.

We used the photometric catalogs and redshifts of the four FFs clusters A2744, M0416, M0717 and M1149 provided by the ASTRODEEP collaboration. The first two clusters have already been analyzed in a previous work C16a, therefore in this paper we only considered the lensing models with versions later than 3.0, which were not adopted in C16a. For other two clusters, we used all available lensing models, and where multiple versions are available we adopted the latest ones.

For the empirical model, at 1σ (2σ) C.L. we have obtained constraints $M_{\rm UV}^{\rm T} \gtrsim -14.6$ ($M_{\rm UV}^{\rm T} \gtrsim -15.2$) at $z \sim 6$. We therefore concluded that we have not yet confirmed the LF turn-over in the data of these four FFs clusters.

For the physically-motivated model we obtained $v_c^* \lesssim 59$ km s^{-1} at 2σ C.L., corresponding to absolute UV magnitude -15.0 at $z = 9.5$ and -14.8 at $z = 5$. Considering the discrepancies between different lensing models, we have $v_c^* \lesssim 45 - 59$

Table 2. Constraints on M_{UV}^T and v_c^*, and the halo mass and absolute UV magnitude corresponding to v_c^* constraints

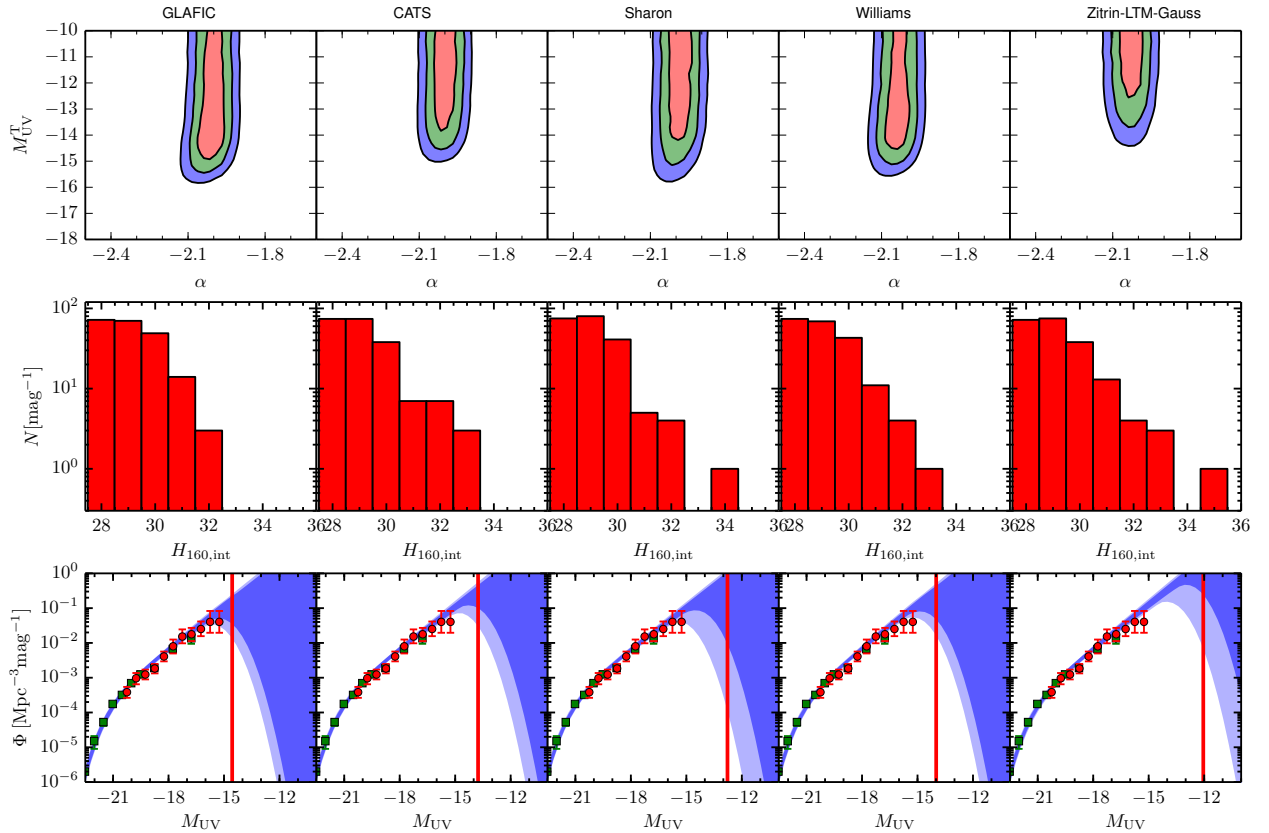|		ALL	GLAFIC	CATS	Sharon	Williams	Zitrin-LTM-Gauss
M_{UV}^T	1σ	$\gtrsim -14.6$	$\gtrsim -14.6$	$\gtrsim -12.9$	$\gtrsim -13.7$	$\gtrsim -14.3$	$\gtrsim -11.8$
	2σ	$\gtrsim -15.2$	$\gtrsim -15.2$	$\gtrsim -14.3$	$\gtrsim -14.7$	$\gtrsim -14.9$	$\gtrsim -13.2$
v_c^*/kms^{-1}	1σ	$\lesssim 50$	$\lesssim 48$	$\lesssim 40$	$\lesssim 45$	$\lesssim 45$	$\lesssim 34$
	2σ	$\lesssim 59$	$\lesssim 56$	$\lesssim 49$	$\lesssim 56$	$\lesssim 54$	$\lesssim 45$
$M_h/M_\odot(z=5)$	1σ	$\lesssim 5.6\times10^9$	$\lesssim 4.9\times10^9$	$\lesssim 2.9\times10^9$	$\lesssim 4.1\times10^9$	$\lesssim 4.1\times10^9$	$\lesssim 1.8\times10^9$
	2σ	$\lesssim 9.2\times10^9$	$\lesssim 7.9\times10^9$	$\lesssim 5.3\times10^9$	$\lesssim 7.9\times10^9$	$\lesssim 7.0\times10^9$	$\lesssim 4.1\times10^9$
$M_{UV}(z=5)$	1σ	$\gtrsim -14.2$	$\gtrsim -14.0$	$\gtrsim -13.2$	$\gtrsim -13.7$	$\gtrsim -13.7$	$\gtrsim -12.4$
	2σ	$\gtrsim -15.0$	$\gtrsim -14.8$	$\gtrsim -14.1$	$\gtrsim -14.8$	$\gtrsim -14.6$	$\gtrsim -13.7$
$M_h/M_\odot(z=9.5)$	1σ	$\lesssim 2.4\times10^9$	$\lesssim 2.1\times10^9$	$\lesssim 1.2\times10^9$	$\lesssim 1.8\times10^9$	$\lesssim 1.8\times10^9$	$\lesssim 7.6\times10^8$
	2σ	$\lesssim 4.0\times10^9$	$\lesssim 3.4\times10^9$	$\lesssim 2.3\times10^9$	$\lesssim 3.4\times10^9$	$\lesssim 3.0\times10^9$	$\lesssim 1.8\times10^9$
$M_{UV}(z=9.5)$	1σ	$\gtrsim -14.0$	$\gtrsim -13.8$	$\gtrsim -13.0$	$\gtrsim -13.6$	$\gtrsim -13.6$	$\gtrsim -12.3$
	2σ	$\gtrsim -14.8$	$\gtrsim -14.6$	$\gtrsim -14.0$	$\gtrsim -14.6$	$\gtrsim -14.4$	$\gtrsim -13.6$

Figure 5. *Top panels:* The constraints on parameters α and M_{UV}^T from five individual lensing models (marked in the panel), "GLAFIC", "CATS", "Sharon", "Williams" and "Zitrin-LTM-Gauss" from the four FFs clusters data in $z\sim 5-7$. *Middle panels:* The sum of the number counts for the four FFs clusters in $z\sim 5-7$ for the five lensing models. *Bottom panels:* The LFs corresponding to constraints at 1σ C.L. (regions filled by deeper colors) and 2σ C.L. (regions filled by lighter colors). To have clear panels we now only plot the B15 (squares) and A15 (circles) data. In the LFs panels we mark the absolute UV magnitudes of the faintest galaxies identified using each lensing model by vertical lines.
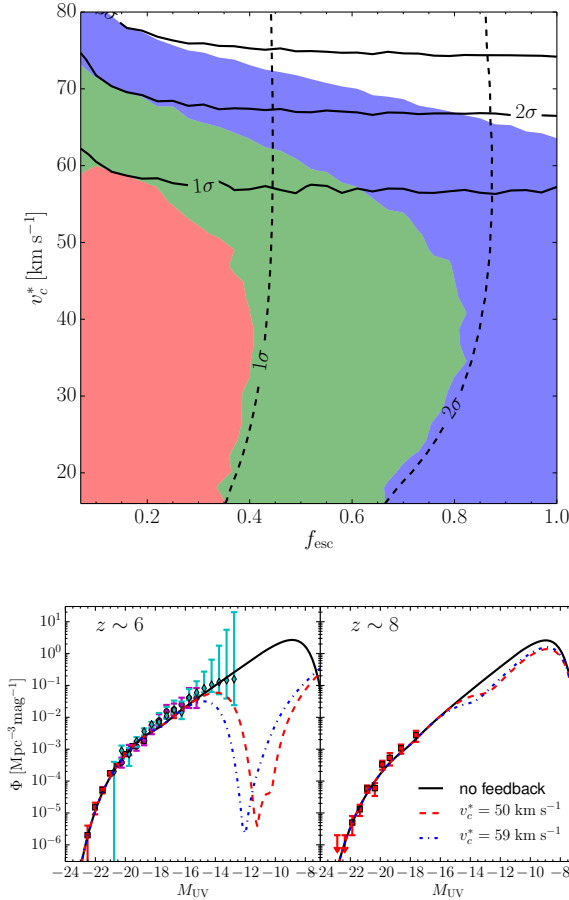
Figure 6. *Top:* The constraints on f_{esc} and v_c^*. We obtain them by using the combination of FFs galaxy number counts and the *Planck* 2016 CMB scattering optical depth $\tau = 0.058 \pm 0.012$ (Planck Collaboration et al. 2016b). Solid contour lines refer to the constraints obtained from galaxy number counts only, dashed lines refer to from the CMB only, and filled regions refer to constraints from their combination. *Bottom:* The LFs that correspond to no feedback, $v_c^* = 50$ and 59 km s^{-1} models at $z \sim 6$ and 8. Filled squares refer to the B15 data at $z \sim 6$ and 8; filled circles refer to A15 data at $z \sim 7$; and filled diamonds refer to B17 data at $z \sim 6$. We always use $f_{esc} = 0.15$ for theoretical LFs in this panel.

km s^{-1}. In all the cases considered, we have not found the lower limit for v_c^*.

All the numerical results of both the empirical model and the physically-motivated model are listed in Tab. 2, and in the physically-motivated model we have translated the v_c^* constraints into the M_{UV} constraints at $z = 5$ and $z = 9.5$ respec-

tively. Although the constraints on v_c^* can be translated into constraints on M_{UV}^T through the luminosity - halo mass relations, we remind that in empirical model the constraints are purely from the galaxy surveys, while in the physically-motivated model the constraints are from both the galaxy surveys and the CMB scattering optical depth. In spite of this, the results of these models are considered consistent in the fiducial case (ALL model in Tab. 2): e.g. $M_{UV}^T \gtrsim -14.6$ vs. $M_{UV}(z = 5) \gtrsim -14.2$.

Thanks to the combined power of gravitational lensing and deep *HST* multi-band imaging we are just starting to observe the faintest galaxy populations likely responsible for reionization. The present analysis and similar ones in the past have not yet found significant evidence of the presence of feedback effects suppressing the formation of galaxies at faint UV magnitudes. This is likely due to the uncertainties and systematics involved in lensing models and in the selection and characterization of distant, faint sources. In this respect, the completion of the FFs survey, and improvements in lensing model accuracy as well as high redshift sample selection enabled by future *JWST* photometric and spectroscopic observations will be crucial for improving our understanding of reionization.

REFERENCES

Acebron, A., Jullo, E., Limousin, M., et al. 2017, MNRAS, 470, 1809

Atek, H., Richard, J., Jauzac, M., et al. 2015a, ApJ, 814, 69, [A15]

Atek, H., Richard, J., Kneib, J.-P., et al. 2015b, ApJ, 800, 18

Bertin, E., & Arnouts, S. 1996, A&AS, 117, 393

Bouwens, R. J., Illingworth, G. D., Oesch, P. A., et al. 2017a, ApJ, 843, 41

—. 2015a, ApJ, 811, 140

Bouwens, R. J., Oesch, P. A., Illingworth, G. D., Ellis, R. S., & Stefanon, M. 2017b, ApJ, 843, 129, [B17]

Bouwens, R. J., Illingworth, G. D., Oesch, P. A., et al. 2015b, ApJ, 803, 34, [B15]

Bradač, M., Schneider, P., Lombardi, M., & Erben, T. 2005, A&A, 437, 39

Bradač, M., Treu, T., Applegate, D., et al. 2009, ApJ, 706, 1201

Brammer, G. B., Marchesini, D., Labbé, I., et al. 2016, ApJS, 226, 6

Castellano, M., Yue, B., Ferrara, A., et al. 2016a, ApJL, 823, L40, [C16a]

Castellano, M., Dayal, P., Pentericci, L., et al. 2016b, ApJL, 818, L3

Castellano, M., Amorín, R., Merlin, E., et al. 2016c, A&A, 590, A31

Ceverino, D., Glover, S. C. O., & Klessen, R. S. 2017, MNRAS, 470, 2791

Choudhury, T. R., & Ferrara, A. 2007, MNRAS, 380, L6

Choudhury, T. R., Ferrara, A., & Gallerani, S. 2008, MNRAS, 385, L58

Dayal, P., Dunlop, J. S., Maio, U., & Ciardi, B. 2013, MNRAS, 434, 1486

Dayal, P., Mesinger, A., & Pacucci, F. 2015, ApJ, 806, 67

Di Criscienzo, M., Merlin, E., Castellano, M., et al. 2017, ArXiv e-prints, arXiv:1706.03790

Diego, J. M., Protopapas, P., Sandvik, H. B., & Tegmark, M. 2005a, MNRAS, 360, 477

Diego, J. M., Sandvik, H. B., Protopapas, P., et al. 2005b, MNRAS, 362, 1247

Diego, J. M., Tegmark, M., Protopapas, P., & Sandvik, H. B. 2007, MNRAS, 375, 958

Diego, J. M., Broadhurst, T., Benitez, N., et al. 2015, MNRAS, 446, 683

Finkelstein, S. L., Ryan, Jr., R. E., Papovich, C., et al. 2015, ApJ, 810, 71

Finlator, K., Prescott, M. K. M., Oppenheimer, B. D., et al. 2017, MNRAS, 464, 1633

Giallongo, E., Grazian, A., Fiore, F., et al. 2015, A&A, 578, A83

Giocoli, C., Moreno, J., Sheth, R. K., & Tormen, G. 2007, MNRAS, 376, 977

Gnedin, N. Y. 2016, ApJL, 825, L17

González-López, J., Bauer, F. E., Romero-Cañizales, C., et al. 2017a, A&A, 597, A41

González-López, J., Bauer, F. E., Aravena, M., et al. 2017b, ArXiv e-prints, arXiv:1704.03007

Grillo, C., Suyu, S. H., Rosati, P., et al. 2015, ApJ, 800, 38

Hoag, A., Huang, K.-H., Treu, T., et al. 2016, ApJ, 831, 182

Huang, K.-H., Ferguson, H. C., Ravindranath, S., & Su, J. 2013, ApJ, 765, 68

Ishigaki, M., Kawamata, R., Ouchi, M., Oguri, M., & Shimasaku, K. 2017, ArXiv e-prints, arXiv:1702.04867, [I17]

Ishigaki, M., Kawamata, R., Ouchi, M., et al. 2015, ApJ, 799, 12

Jauzac, M., Jullo, E., Kneib, J.-P., et al. 2012, MNRAS, 426, 3369

Jauzac, M., Clément, B., Limousin, M., et al. 2014, MNRAS, 443, 1549

Jauzac, M., Richard, J., Jullo, E., et al. 2015, MNRAS, 452, 1437

Johnson, T. L., Sharon, K., Bayliss, M. B., et al. 2014, ApJ, 797, 48

Jullo, E., & Kneib, J.-P. 2009, MNRAS, 395, 1319

Jullo, E., Kneib, J.-P., Limousin, M., et al. 2007, New Journal of Physics, 9, 447

Kawamata, R., Ishigaki, M., Shimasaku, K., et al. 2017, ArXiv e-prints, arXiv:1710.07301

Kawamata, R., Oguri, M., Ishigaki, M., Shimasaku, K., & Ouchi, M. 2016, ApJ, 819, 114

Laporte, N., Infante, L., Troncoso Iribarren, P., et al. 2016, ApJ, 820, 98

Liesenborgs, J., De Rijcke, S., & Dejonghe, H. 2006, MNRAS, 367, 1209

Liu, C., Mutch, S. J., Angel, P. W., et al. 2016, MNRAS, 462, 235

Livermore, R. C., Finkelstein, S. L., & Lotz, J. M. 2017, ApJ, 835, 113, [L17]

Lotz, J. M., Koekemoer, A., Coe, D., et al. 2017, ApJ, 837, 97

Madau, P., & Haardt, F. 2015, ApJL, 813, L8

Mashian, N., Oesch, P. A., & Loeb, A. 2016, MNRAS, 455, 2101

Mason, C. A., Trenti, M., & Treu, T. 2015, ApJ, 813, 21

McLure, R. J., Dunlop, J. S., Bowler, R. A. A., et al. 2013, MNRAS, 432, 2696

Menci, N., Merle, A., Totzauer, M., et al. 2017, ApJ, 836, 61

Menci, N., Sanchez, N. G., Castellano, M., & Grazian, A. 2016, ApJ, 818, 90

Meneghetti, M., Natarajan, P., Coe, D., et al. 2017, MNRAS, 472, 3177

Merlin, E., Fontana, A., Ferguson, H. C., et al. 2015, A&A, 582, A15

Merlin, E., Bourne, N., Castellano, M., et al. 2016a, A&A, 595, A97

Merlin, E., Amorín, R., Castellano, M., et al. 2016b, A&A, 590, A30

Merten, J., Cacciato, M., Meneghetti, M., Mignone, C., & Bartelmann, M. 2009, A&A, 500, 681

Merten, J., Coe, D., Dupke, R., et al. 2011, MNRAS, 417, 333

Mitra, S., Choudhury, T. R., & Ferrara, A. 2016, ArXiv e-prints, arXiv:1606.02719

Mohammed, I., Liesenborgs, J., Saha, P., & Williams, L. L. R. 2014, MNRAS, 439, 2651

Ogrean, G. A., van Weeren, R. J., Jones, C., et al. 2015, ApJ, 812, 153

—. 2016, ApJ, 819, 113

Oguri, M. 2010, PASJ, 62, 1017

Planck Collaboration, Ade, P. A. R., Aghanim, N., et al. 2016a,
    A&A, 594, A13

Planck Collaboration, Adam, R., Aghanim, N., et al. 2016b, A&A,
    596, A108

Priewe, J., Williams, L. L. R., Liesenborgs, J., Coe, D., & Rodney,
    S. A. 2017, MNRAS, 465, 1030

Richard, J., Jauzac, M., Limousin, M., et al. 2014, MNRAS, 444,
    268

Robertson, B. E., Ellis, R. S., Furlanetto, S. R., & Dunlop, J. S.
    2015, ApJL, 802, L19

Robertson, B. E., Furlanetto, S. R., Schneider, E., et al. 2013, ApJ,
    768, 71

Salvaterra, R., Ferrara, A., & Dayal, P. 2011, MNRAS, 414, 847

Salvaterra, R., Maio, U., Ciardi, B., & Campisi, M. A. 2013,
    MNRAS, 429, 2718

Sebesta, K., Williams, L. L. R., Mohammed, I., Saha, P., &
    Liesenborgs, J. 2016, MNRAS, 461, 2126

Sun, G., & Furlanetto, S. R. 2016, MNRAS, 460, 417

Tacchella, S., Trenti, M., & Carollo, C. M. 2013, ApJL, 768, L37

Trenti, M., Stiavelli, M., Bouwens, R. J., et al. 2010, ApJL, 714,
    L202

van Weeren, R. J., Ogrean, G. A., Jones, C., et al. 2017, ApJ, 835,
    197

Weisz, D. R., Johnson, B. D., & Conroy, C. 2014, ApJL, 794, L3

Xu, H., Wise, J. H., Norman, M. L., Ahn, K., & O'Shea, B. W.
    2016, ApJ, 833, 84

Yue, B., Ferrara, A., Vanzella, E., & Salvaterra, R. 2014, MNRAS,
    443, L20

Yue, B., Ferrara, A., & Xu, Y. 2016, MNRAS, 463, 1968, [Y16]

Zitrin, A., Broadhurst, T., Umetsu, K., et al. 2009, MNRAS, 396,
    1985

Zitrin, A., Meneghetti, M., Umetsu, K., et al. 2013, ApJL, 762, L30

APPENDIX

A. THE LIST OF OUR SELECTED GALAXY SAMPLES

Table A1. Our selected galaxies in ASTRODEEP catalogs. The SEDs, cutouts and all ancillary information could be found on the ASTRODEEP CDS interface at http://astrodeep.u-strasbg.fr/ff/.

A2744			M0416			M0717			M1149		
ID	H_{160}	z	ID	H_{160}	z	ID	H_{160}	z	ID	H_{160}	z
54	27.81± 0.15	5.10± 0.11	73	28.03± 0.15	6.07± 0.07	69	27.09± 0.12	5.18± 0.09	354	28.03± 0.15	5.66± 0.14
62	25.18± 0.05	6.13± 0.03	132	28.11± 0.26	5.03± 0.08	75	28.56± 0.22	5.19± 0.47	362	27.14± 0.09	5.61± 0.17
67	27.17± 0.12	5.54± 0.07	141*	27.77± 0.13	6.68± 0.99	82	26.77± 0.08	6.05± 0.05	396	28.35± 0.18	6.92± 1.01
73	26.50± 0.05	6.85± 0.04	143*	26.97± 0.08	6.55± 1.00	96	27.44± 0.19	7.90± 0.04	402	28.17± 0.19	6.38± 0.08
145	27.08± 0.13	5.87± 0.30	158	28.00± 0.24	8.27± 0.10	151	27.65± 0.18	5.43± 0.05	433	27.75± 0.13	6.16± 0.02
189	28.01± 0.14	5.68± 0.15	201*	28.70± 0.21	5.70± 2.45	165	27.52± 0.17	5.49± 3.24	448	28.66± 0.26	5.05± 0.19
203	28.59± 0.19	5.53± 0.03	220	27.74± 0.15	5.82± 0.06	222*	27.53± 0.26	5.05± 0.85	531	27.92± 0.14	6.56± 0.13
222	27.23± 0.11	5.02± 0.03	246	28.81± 0.40	6.41± 0.02	248*	27.73± 0.16	5.42± 0.53	546	28.22± 0.26	5.01± 0.03
263	27.08± 0.12	5.25± 0.09	247*	27.22± 0.10	7.13± 0.11	272	28.29± 0.20	5.66± 0.12	574	28.01± 0.20	5.21± 2.12
292*	27.59± 0.10	5.38± 0.03	265	27.58± 0.21	5.24± 2.00	336	27.10± 0.10	6.10± 0.05	708	28.10± 0.19	5.14± 0.11
321	28.83± 0.19	5.71± 0.03	286*	28.20± 0.17	8.14± 0.18	356	28.45± 0.23	6.16± 0.12	905	25.93± 0.03	5.05± 0.10
345*	28.46± 0.17	5.35± 0.13	354	28.41± 0.23	5.24± 0.05	361	26.17± 0.10	6.45± 0.03	942*	26.90± 0.09	6.25± 3.93
379	28.15± 0.16	6.61± 0.21	355	27.87± 0.17	6.24± 0.03	374*	27.37± 0.17	6.25± 0.08	945	27.92± 0.13	6.68± 0.09
389	27.44± 0.10	5.36± 0.08	465	27.40± 0.11	5.33± 0.09	392*	27.54± 0.24	6.03± 0.20	1144	27.96± 0.14	5.41± 0.19
394	28.40± 0.17	6.60± 0.06	513*	28.12± 0.21	6.79± 2.58	471	26.68± 0.08	6.53± 0.03	1180	27.31± 0.14	7.17± 0.14
397	27.17± 0.10	6.31± 0.11	524	28.11± 0.15	5.20± 0.07	510	26.87± 0.08	6.46± 0.03	1226	28.35± 0.17	9.14± 3.51
409	28.32± 0.19	7.66± 0.01	637*	27.69± 0.13	6.41± 0.20	511	27.36± 0.11	5.20± 0.06	1243	27.44± 0.11	5.92± 0.07
411	28.01± 0.17	7.44± 0.05	678	28.48± 0.19	5.37± 0.03	630*	27.31± 0.10	5.44± 0.04	1268	28.37± 0.17	5.20± 0.08
422	28.35± 0.24	5.55± 0.03	726	26.76± 0.06	8.32± 0.07	636	28.19± 0.23	5.34± 0.18	1388	27.58± 0.17	7.29± 0.25
425	26.76± 0.07	5.24± 0.07	915	27.56± 0.23	5.31± 1.93	640	26.87± 0.09	6.02± 0.02	1428	28.34± 0.17	6.89± 0.07
437	28.67± 0.22	5.87± 0.09	1024	28.06± 0.16	7.49± 0.07	653	24.65± 0.01	5.42± 0.07	1434	28.40± 0.21	6.39± 0.15
446	27.60± 0.13	6.02± 0.02	1074	26.68± 0.10	5.78± 2.23	774	28.07± 0.16	5.93± 0.09	1494	26.11± 0.05	5.76± 0.09
466	27.12± 0.14	5.75± 0.02	1105	27.90± 0.17	5.29± 2.01	790	25.52± 0.02	5.78± 0.11	1513	28.75± 0.32	8.54± 0.01
475	27.82± 0.19	5.10± 0.10	1164	28.55± 0.24	5.96± 0.09	797	25.31± 0.04	5.97± 2.29	1529	27.38± 0.10	5.08± 0.06
491	28.58± 0.25	5.16± 0.05	1260	28.59± 0.21	5.24± 0.01	813	28.20± 0.18	5.90± 0.09	1733	26.82± 0.20	8.76± 0.85
535	28.09± 0.25	5.12± 0.49	1333	26.68± 0.06	5.16± 0.09	880	27.04± 0.12	5.19± 0.59	1751	28.12± 0.41	8.32± 0.04
548*	28.42± 0.20	8.56± 0.02	1405	26.33± 0.06	5.16± 0.04	922	26.86± 0.10	5.49± 0.03	1758	26.65± 0.18	8.96± 4.24
560	29.03± 0.22	5.18± 0.11	1457	28.64± 0.28	6.07± 0.24	955	24.52± 0.03	5.54± 0.26	1970	28.08± 0.30	5.41± 2.38
561	26.78± 0.10	6.37± 0.02	1494	27.57± 0.21	7.08± 0.03	1028	27.67± 0.12	5.65± 0.08	2014	27.80± 0.24	6.61± 0.05
626	27.48± 0.09	5.55± 0.01	1589	27.12± 0.16	7.50± 0.12	1095	26.52± 0.11	5.73± 0.07	2316	28.81± 0.27	7.93± 0.04
657	28.55± 0.29	9.33± 0.07	1608	27.24± 0.23	5.03± 0.21	1178	26.82± 0.06	6.00± 0.05	2364	28.81± 0.23	5.71± 0.06
707	29.01± 0.23	6.59± 0.04	1614	27.15± 0.18	6.29± 0.21	1286	27.41± 0.19	5.05± 0.26	2368	26.60± 0.07	5.94± 0.06

709	28.27± 0.27	6.31± 0.02	1632	28.17± 0.36	6.08± 2.29	1333	28.15± 0.27	5.22± 0.33	2410	27.10± 0.10	6.00± 0.03
742	27.24± 0.08	6.55± 0.26	1635	27.24± 0.20	5.61± 2.31	1363*	26.50± 0.09	5.16± 0.74	2535	26.91± 0.07	5.54± 0.09
808	26.60± 0.07	5.36± 0.01	1660	26.83± 0.12	5.51± 0.44	1398	26.48± 0.11	5.17± 0.07	2619	27.09± 0.07	5.79± 0.11
809	27.55± 0.11	5.42± 0.04	1706	26.91± 0.11	5.42± 0.12	1481	26.92± 0.10	5.15± 2.19	2747	28.15± 0.23	6.17± 0.04
834	26.40± 0.10	5.58± 0.07	1815	27.19± 0.16	7.22± 2.78	1563	28.31± 0.20	6.86± 0.03	2764	27.18± 0.10	5.67± 0.07
835	27.69± 0.18	6.15± 0.09	1827	27.31± 0.14	5.91± 0.02	1584	28.28± 0.19	6.22± 0.04	2792	28.14± 0.16	7.18± 0.11
855	27.60± 0.13	6.02± 0.03	1829	28.65± 0.20	5.96± 0.01	1622	27.60± 0.12	6.25± 0.03	2833	27.70± 0.12	7.26± 0.09
863	27.01± 0.07	5.87± 0.06	1900	29.14± 0.91	5.17± 0.30	1737	26.89± 0.13	6.04± 0.07	2950*	28.19± 0.21	8.62± 3.19
902	29.02± 0.53	5.21± 0.06	1909	27.86± 0.21	5.43± 2.28	1772	24.55± 0.03	5.14± 0.10	2966	27.51± 0.11	6.40± 0.03
921	28.74± 0.49	5.28± 0.09	1956	28.16± 0.16	7.81± 0.04	1802	25.87± 0.05	5.53± 0.04	3027	28.03± 0.16	5.83± 0.01
943	28.18± 0.22	6.97± 0.07	1997	27.56± 0.17	8.10± 0.05	1841	27.81± 0.13	5.74± 0.05	3073	28.13± 0.18	5.10± 0.10
945	28.61± 0.29	5.62± 0.19	2018*	28.26± 0.15	5.31± 0.84	1868	25.49± 0.02	5.64± 2.39	3162	27.67± 0.14	6.07± 0.15
1012	28.31± 0.13	5.24± 0.41	2067	28.19± 0.23	5.07± 0.20	1874*	27.27± 0.11	5.48± 0.08	3195*	28.71± 0.48	6.14± 3.67
1020	29.06± 0.62	5.70± 0.07	2157	28.34± 0.17	5.36± 0.09	2156	25.26± 0.05	5.50± 2.31	3236*	27.12± 0.23	9.11± 1.04
1028*	27.62± 0.20	7.08± 0.14	2169	28.09± 0.15	5.97± 0.03	2191	27.31± 0.13	5.46± 0.26	3374	26.95± 0.12	7.43± 0.09
1032	28.21± 0.14	7.09± 0.08	2179	26.69± 0.07	6.25± 0.03	2204	27.19± 0.07	5.38± 2.16			
1051	27.11± 0.21	6.56± 0.07	2190	28.25± 0.18	5.40± 2.19	2302	27.01± 0.14	5.37± 0.10			
1273	27.31± 0.11	6.61± 0.02	2196	28.56± 0.29	5.91± 0.06	2312	26.45± 0.05	6.12± 0.04			
1333	27.23± 0.09	5.64± 0.03	2204	26.99± 0.13	6.30± 0.03	2321	27.76± 0.23	5.10± 0.14			
1387*	27.29± 0.11	6.72± 0.23	2236	27.67± 0.13	5.97± 0.03	2368*	26.54± 0.16	5.75± 0.08			
1399	26.94± 0.08	5.11± 0.01	2240	27.96± 0.07	5.75± 0.07	2429	28.15± 0.21	5.05± 0.10			
1450	28.30± 0.26	5.48± 0.25	2315*	27.46± 0.15	5.13± 0.06	2442	26.66± 0.08	5.21± 0.11			
1516	28.15± 0.15	5.14± 0.06	2323	28.40± 0.18	5.18± 0.03	2520*	27.20± 0.17	9.14± 1.04			
1622	28.94± 0.39	5.87± 0.06	2324	28.15± 0.25	6.29± 0.02	2575	28.24± 0.26	6.17± 0.23			
1686	28.06± 0.16	5.02± 0.06	2337	27.30± 0.16	6.16± 0.03	2584	28.61± 0.30	5.17± 1.83			
1718	24.03± 0.01	6.21± 0.09	2385	28.09± 0.16	8.83± 0.03	2585	27.63± 0.21	5.69± 0.12			
1747*	27.69± 0.10	5.20± 2.53	2411	28.65± 0.20	5.91± 0.05	2625	27.41± 0.21	5.70± 0.15			
1762	28.65± 0.18	5.25± 0.01	2462	28.39± 0.18	5.69± 0.03	2656	28.90± 0.61	5.59± 2.50			
1968*	27.38± 0.09	5.19± 0.08	2554	27.81± 0.21	5.90± 0.03	2667*	26.83± 0.09	5.27± 0.37			
1990	27.99± 0.21	7.07± 0.13	2555	27.52± 0.20	6.00± 0.02	2730	26.90± 0.12	5.36± 0.19			
2002	28.25± 0.16	6.46± 0.02				2745	26.83± 0.12	5.06± 0.24			
2007	28.70± 0.29	5.82± 0.07				2782	27.38± 0.23	5.27± 2.23			
2036	26.95± 0.07	8.32± 0.03				2799	28.40± 0.26	5.22± 0.03			
2037	28.22± 0.15	5.08± 0.07				2840	28.04± 0.21	5.18± 0.20			
2066*	27.82± 0.16	5.95± 2.34				2843	26.01± 0.06	5.47± 2.23			
2112	28.45± 0.17	5.07± 0.07				2852	27.67± 0.14	5.08± 0.22			
2181	28.01± 0.21	5.17± 0.14				2860	28.02± 0.25	5.37± 0.06			
2202	27.69± 0.11	5.86± 0.01				2883	25.91± 0.06	6.37± 0.04			
2241	28.33± 0.16	6.84± 0.04				2902	27.71± 0.23	6.25± 0.04			
2257	28.62± 0.18	7.53± 0.43				3015	28.53± 0.25	5.76± 0.42			
2261	27.29± 0.10	7.97± 0.10				3017	27.66± 0.18	5.04± 0.69			
2287	27.97± 0.16	8.50± 0.94				3066	28.62± 0.25	6.24± 0.01			

2316	27.98± 0.19	7.66± 0.02			3067	27.21± 0.15	5.97± 0.12
2325	28.54± 0.18	5.36± 0.03			3076*	27.36± 0.14	9.19± 1.04
2338	28.86± 0.22	6.87± 0.04					
2346	26.78± 0.06	7.79± 0.04					
2380	27.71± 0.22	7.93± 0.14					
2388	27.57± 0.21	5.17± 0.09					
2434	28.40± 0.16	5.82± 0.07					
2446	28.05± 0.15	5.73± 0.08					
2452	27.00± 0.09	5.74± 0.07					
2471	28.72± 0.18	5.66± 0.07					
2544	27.03± 0.11	5.26± 0.08					
2567*	28.98± 0.27	5.10± 0.15					
2595	27.14± 0.10	6.33± 0.05					

[*] Some objects with possibly problematic SEDs are marked with "*". They are mostly objects showing some flux below the Lyman break, plus some sources detected only in one band. However, we verified that there are no solid reasons to remove them and the photometric redshift solutions appear to be reliable. In particular, the cases of detected flux below the break are mostly due to some contamination from nearby sources or to noise or background fluctuations.
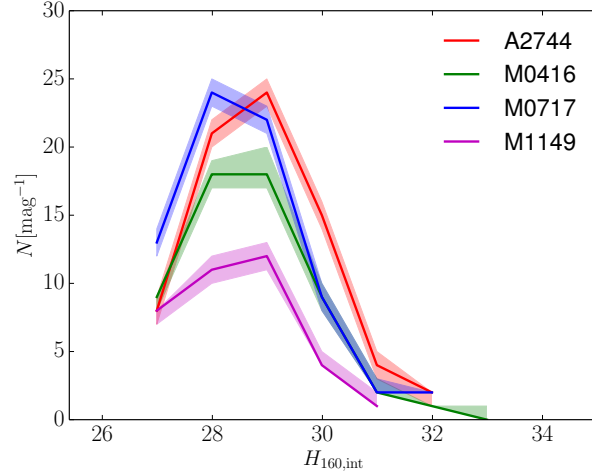
Figure 7. The number counts and 1σ variance induced by the photometric errors for the four FFs clusters.

B. THE INFLUENCE OF PHOTOMETRIC ERRORS

In this section we investigate the influence of the photometric errors on the final constraints on the turn-over magnitude. For each galaxy with $5.0 < z < 7.0$, according to its H_{160} and photometric error, we randomly assign a new H_{160} from the Gaussian probability distribution. We then get the corresponding new demagnified magnitude and build new number counts. For each galaxy we make 10000 random realizations and finally we have the 10000 number count realizations. Based on these realizations we get the corresponding 1σ variance of the number counts rise from the photometric errors. The results for the four FFs clusters are shown in Fig. 7.

We then obtain the new constraints on the turn-over magnitude by using the 1σ lower and upper limit of the number counts respectively. Using the lower limit, we have $M_{\mathrm{UV}}^{\mathrm{T}} > -14.8$ and $M_{\mathrm{UV}}^{\mathrm{T}} > -15.4$) at 1 and 2 σ C.L. respectively; using the upper limit, we have $M_{\mathrm{UV}}^{\mathrm{T}} > -14.1$ and $M_{\mathrm{UV}}^{\mathrm{T}} > -14.8$ respectively at 1 and 2 σ C.L.. We conclude that the influence of the photometric errors on the final constraints is modest.